Frontiers of Information Technology & Electronic Engineering
www.jzus.zju.edu.cn; engineering.cae.cn; www.springerlink.com
ISSN 2095-9184 (print); ISSN 2095-9230 (online)
E-mail: jzus@zju.edu.cn

A lightweight clutter suppression algorithm for passive bistatic radar*#

Yong WU[1], Luo ZUO‡[2], Dongliang PENG[3], Zhikun CHEN[3]

[1]*Intelligent Transportation School, Zhejiang Institute of Communications, Hangzhou 311112, China*
[2]*Guangzhou Institute of Technology, Xidian University, Guangzhou 510555, China*
[3]*School of Automation, Hangzhou Dianzi University, Hangzhou 310018, China*
E-mail: wuyong@zjvtit.edu.cn; zuoluo@xidian.edu.cn; dlpeng@hdu.edu.cn; czk@hdu.edu.cn

Received Dec. 22, 2023; Revision accepted Apr. 7, 2024; Crosschecked Sept. 19, 2024

Abstract: In passive bistatic radar, the computational efficiency of clutter suppression algorithms remains low, due to continuous increases in bandwidth for potential illuminators of opportunity and the use of multi-source detection frameworks. Accordingly, we propose a lightweight version of the extensive cancellation algorithm (ECA), which achieves clutter suppression performance comparable to that of ECA while reducing the computational and space complexities by at least one order of magnitude. This is achieved through innovative adjustments to the reference signal subspace matrix within the ECA framework, resulting in a redefined approach to the computation of the autocorrelation matrix and cross-correlation vector. This novel modification significantly simplifies the computational aspects. Furthermore, we introduce a dimension-expanding technique that streamlines clutter estimation. Overall, the proposed method replaces the computation-intensive aspects of the original ECA with fast Fourier transform (FFT) and inverse FFT operations, and eliminates the construction of the memory-intensive signal subspace. Comparing the proposed method with ECA and its batched version (ECA-B), the central advantages are more streamlined implementation and minimal storage requirements, all without compromising performance. The efficacy of this approach is demonstrated through both simulations and field experimental results.

Key words: Passive bistatic radar; Clutter suppression; Extensive cancellation algorithm; Computational complexity; Space complexity
https://doi.org/10.1631/FITEE.2300859 **CLC number:** TN95

1 Introduction

Passive radar, commonly referred to as passive bistatic radar (PBR), is a passive sensor that uses existing illuminators of opportunity present in the environment, such as signals emitted by broadcasting, communication, television, or navigation transmitters (Mahfoudia et al., 2019; Pastina et al., 2021; Lestari et al., 2022; Samczyński et al., 2022; Zhang et al., 2023). Instead of relying on dedicated radar transmitters, PBR detects and tracks targets by capitalizing on the bistatic radar principle, wherein the receiver and transmitter are strategically positioned at separate locations. This approach eliminates the need to deploy transmitting stations and facilitates covert reception. Consequently, PBR has emerged as an alluring choice for surveillance and military applications (Sun et al., 2021; Fränken et al., 2022), with a focus on anti-jamming,

‡ Corresponding author
* Project supported by the Zhejiang Provincial Natural Science Foundation of China (No. LZ23F030002), the Science and Technology Program of Zhejiang Provincial Department of Transportation (No. 2024012), and the Talent Funding Project of Zhejiang Institute of Communications (Nos. 822321KY0127 and 2024JK05)
# Electronic supplementary materials: The online version of this article (https://doi.org/10.1631/FITEE.2300859) contains supplementary materials, which are available to authorized users
ORCID: Yong WU, https://orcid.org/0009-0008-8580-5196; Luo ZUO, https://orcid.org/0000-0002-3434-6312

anti-stealth, and low-observability properties. Despite the potential advantages of PBR, the bistatic geometry configuration and often-non-cooperative transmitters pose significant challenges to its detection performance. Therefore, there is a demand for signal processing algorithms that can enhance the object detection ability of PBR. The foremost goal of such algorithms is the removal of direct path and multipath clutter in the surveillance signal (Garry et al., 2017), since these factors can severely compromise the precision of object detection.

In a typical PBR configuration, two distinct channels, the reference channel and the surveillance channel, are harnessed for signal reception. Usually, the reference channel is dedicated to capturing the direct path signal emitted by the transmitting station, while the surveillance channel is tasked with capturing emission signals originating from the targets of interest. In real-world scenarios, the surveillance signal consists not just of echoes from targets, but also direct path, multipath, and noise signals. Among these signal components, clutter exhibits the highest energy level. Consequently, filtering out clutter from the surveillance signal is a common early data processing step—a process termed clutter suppression. Following clutter suppression, the energy that emanates from targets is systematically aggregated by computing the cross-ambiguity function (CAF) (Palmer et al., 2011) between the residual surveillance signal and its time-delayed reference signal counterpart. This processing is commonly referred to as range-Doppler (RD) processing. Finally, the detection of targets is realized through the implementation of the constant false alarm rate (CFAR) detection method. Clutter suppression plays a pivotal role in the target detection ability of PBR technology. Thus, the design of an accurate and efficient clutter suppression method is vital for improved results.

Due to the critical significance of clutter suppression in the domain of PBR development, a diverse array of clutter suppression algorithms have been proposed. These algorithms can be broadly classified into two categories. The first category encompasses closed-loop feedback mechanisms, which include widely used algorithms such as least mean squares (LMS) (Cardinali et al., 2007), its variations (Bernaschi et al., 2012; Palmer and Searle, 2012; Attalah et al., 2019), and various iterations of recursive least squares (RLS) (Farhang-Boroujeny, 2013; Bolvardi et al., 2015). These adaptive algorithms have demonstrated superiority in dynamic clutter environments (Garry et al., 2017), yet their iterative nature poses limitations on their applicability, particularly within PBR systems necessitating real-time responsiveness. The second category comprises open-loop algorithms, among which the extensive cancellation algorithm (ECA) (Colone et al., 2009, 2023; Lyu and Ding, 2022) holds a predominant role, finding broad applications in diverse PBR scenarios. In contrast to LMS and RLS, ECA eliminates the need for iterative calculations and is more amenable to acceleration, garnering significant attention from researchers due to its high performance. With this in mind, we use ECA as a base upon which to build our method. The core concept of ECA is to reduce clutter by projecting the surveillance signal onto the orthogonal subspace created by the reference signal and its time-delayed cells. However, due to the need to construct a clutter subspace in ECA that is related to a coherent processing interval (CPI) (Moscardini et al., 2015; Kuschel et al., 2019) and the actual clutter's degree of freedom, ECA still necessitates substantial computational operations and large storage capacity. Additionally, with the increasing bandwidth of potential illuminating PBR signals and the commonly adopted multi-source detection architecture, the computational efficiency of ECA has gradually become a limiting factor for its practical engineering applications, despite its relatively strong performance.

To mitigate ECA's computational complexity, variations on the algorithm have emerged which are generally classified into two groups. The first group involves direct modification to ECA itself, while the second group uses emerging hardware for acceleration. In terms of ECA improvements, a batched version of ECA through signal segmentation (ECA-B) (Colone et al., 2009; Ansari et al., 2016) was introduced to reduce computational load. However, this approach introduces periodic peaks in specific scenarios, such as low Doppler shifts or slow-moving targets (Zuo et al., 2021). To address this limitation, a sliding approach (ECA-S) employing overlapping data segmentation was proposed (Colone et al., 2016, 2022; Martelli et al., 2020). ECA-S strikes a balance between the performance of ECA and ECA-B, but necessitates

more computations due to its sliding window component. Thus, an extended ECA-B variant was developed, dividing the entire signal into more batches than ECA-B while maintaining robust cancellation performance (Fu et al., 2018). Furthermore, another efficient version of ECA has been proposed which addresses the issue of reduced Doppler resolution following signal segmentation (Miao et al., 2021). Although these methods offer acceleration to ECA, their computational complexity remains at the same order, due to the necessity for constructing high-dimensional clutter subspaces. In essence, for these approaches to significantly alleviating ECA's computational load, the entire signal must be divided into more segments; however, this often results in a decrease in clutter suppression performance. On the other hand, leveraging specialized hardware for brute-force acceleration is a more direct avenue for enhancement. Specifically, a fast implementation of ECA based on field programmable gate arrays (FPGAs) achieved an 18-fold speed increase over central processing units (CPUs) (Jarrah and Jamali, 2016a). Additionally, implementations of ECA and its variants on graphical processing units (GPUs), which employ parallel and pipelining strategies, have achieved substantial acceleration, surpassing traditional serial implementations by orders of magnitude (John et al., 2011; Jarrah and Jamali, 2016b).

Although the aforementioned methods have yielded promising results, these methods improve the efficiency of ECA at the cost of either compromises to performance or reliance on specific hardware configurations. Methods that efficiently curtail the computational complexity of ECA by a factor of tenfold or more, while simultaneously upholding performance and minimizing additional dependencies, remain notably scarce. Therefore, there is a disparity between the improvement of ECA's efficiency and the preservation of its performance. To bridge this gap, we introduce a lightweight ECA called ECA-L. ECA-L works through circular convolutions and circular matrix processing, leveraging fast Fourier transforms (FFTs) and inverse FFTs (IFFTs) to fundamentally reshape the construction of reference subspaces and large-scale matrix computations. This transformation yields an order-of-magnitude reduction in both computational workload and storage space requirement compared to the traditional ECA, while retaining high performance. Furthermore, the proposed method performs well in practical scenarios of ECA thanks to its lightweight computational nature, demonstrating its suitability for real-world applications. Our proposed method makes improvements on existing methods in the following ways:

Despite introducing only subtle structural modifications to the ECA framework, the computational efficiency and storage requirements are improved dramatically. In contrast to the prevailing methods of data segmentation (Colone et al., 2009), these distinctive refinements offer a novel vantage point for prospective investigations into analogous techniques.

Using circular convolutions and circular matrices, the extensive matrix multiplications inherent in ECA can be substituted with FFTs and IFFTs, thereby significantly improving its computational efficiency. Moreover, compared to existing methods (Colone et al., 2009, 2022; Moscardini et al., 2015), this substitution operation retains higher performance.

In contrast to traditional ECA (Colone et al., 2009) and its variants (Moscardini et al., 2015; Colone et al., 2016; Fu et al., 2018), which necessitate the creation of a projection subspace for the reference signal (incurring a substantial storage overhead), the proposed approach introduces a virtual projection subspace. Notably, practical storage allocation is unnecessary for this virtual subspace, leading to a space complexity reduction of one to two orders of magnitude. This reduction in space complexity could enable a wider array of illuminating signals to be used for target detection.

For ease of reading and understanding, descriptions of commonly used notations are provided in Table 1.

2 Signal model and ECA and ECA-B approaches

In this section, we present the received signal model for PBR. Subsequently, we delve into the baseline algorithm employed for clutter suppression, specifically the ECA method, along with its batched variant.

2.1 Signal model

The geometric configuration of a typical PBR system is depicted in Fig. 1. In this setup, both the transmitter and receiver are stationary. The transmitter

Table 1 Important notations

Notation	Description
Uppercase italic & bold letters	Matrices
Lowercase italic & bold letters	Vectors
$(\cdot)^*$	Conjugate operation
$(\cdot)^{\mathrm{H}}$	Conjugate transpose operation
$(\cdot)^{\mathrm{T}}$	Transpose operation
$*$	Convolution operator
$\boldsymbol{s}_{\mathrm{ref}}$	Original reference signal
$\boldsymbol{s}_{\mathrm{sur}}$	Original surveillance signal
$\tilde{\boldsymbol{s}}_{\mathrm{sur}}$	Residual surveillance signal after performing ECA
$\tilde{\boldsymbol{s}}_{\mathrm{sur}}^{\mathrm{ECA\text{-}B}}$	Residual surveillance signal after performing ECA-B
$\tilde{\boldsymbol{s}}_{\mathrm{ECA}_b}$	Segment of $\tilde{\boldsymbol{s}}_{\mathrm{sur}}^{\mathrm{ECA\text{-}B}}$
$\boldsymbol{R}_x$	Autocorrelation matrix in ECA-L
$\hat{\boldsymbol{s}}_{\mathrm{ref}}$	Reverse sequence vector of $\boldsymbol{s}_{\mathrm{ref}}$
$\boldsymbol{r}_x$	Row element vector of $\boldsymbol{R}_x$
$\tilde{\boldsymbol{r}}_x$	Simplification of $\boldsymbol{r}_x$ to facilitate the calculation
$\boldsymbol{r}_x^{\mathrm{aux}}$	Auxiliary vector composed of $\boldsymbol{r}_x$ to facilitate the calculation of $\boldsymbol{R}_x$
$\boldsymbol{r}_{\mathrm{c}}$	Cross-correlation vector in ECA-L
$\tilde{\boldsymbol{r}}_{\mathrm{c}}$	Auxiliary vector to facilitate the calculation of $\boldsymbol{r}_{\mathrm{c}}$
$\boldsymbol{s}_{\mathrm{sur}}^{\mathrm{c}}$	Estimated clutter vector in ECA-L
$\bar{\boldsymbol{s}}_{\mathrm{sur}}^{\mathrm{c}}$	Equivalent of $\boldsymbol{s}_{\mathrm{sur}}^{\mathrm{c}}$ to facilitate the acquisition of $\boldsymbol{s}_{\mathrm{sur}}^{\mathrm{c}}$
$\boldsymbol{\alpha}$	Projection weight vector
$\hat{\boldsymbol{\alpha}}$	Dimension expansion of $\boldsymbol{\alpha}$ filled with zeros

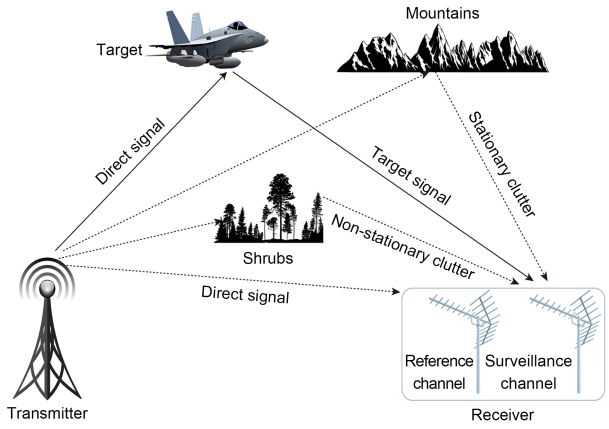

Fig. 1 Sketch diagram of a passive bistatic radar (PBR) system

is an existing illuminator of opportunity present in the environment, while the receiver is the designed component, typically consisting of two distinct receiving channels. One channel functions as the reference channel, which is primarily designed to capture the direct signal emitted by the illuminator of opportunity. Conversely, the other channel, termed the surveillance channel, is primarily designated for receiving target echoes. However, this channel will also inevitably pick up multipath clutter. This multipath clutter consists primarily of stationary clutter reflected from immobile objects, like mountains and buildings, alongside non-stationary clutter emitted by slightly moving objects, such as foliage, among which stationary clutter dominates. The primary distinction between stationary and non-stationary clutter lies in the fact that the Doppler frequency of non-stationary clutter is non-zero. While the forthcoming method can address both types of clutter, mitigating non-stationary clutter requires additional modifications which lie beyond the scope of this study. Hence, we focus on filtering static clutter from the surveillance channel of ground-based passive radar. Within this framework, the statistical properties of stationary clutter are presumed to remain constant throughout the CPI, which is a fundamental assumption in passive radar clutter suppression. For consistency in the subsequent analysis, we denote the signal obtained

from the reference channel as the reference signal, while the signal acquired from the surveillance channel is referred to as the surveillance signal. After undergoing a series of operations including analog-to-digital conversion, digital down-conversion, and filtering extraction, the initial reference signal can be effectively represented as

$$s_{\mathrm{ref}}[n]=a_{\mathrm{ref}}d[n]+z_{\mathrm{ref}}[n],\quad n=1,2,\cdots,N, \tag{1}$$

where $s_{\mathrm{ref}}[n]$ denotes the n^{th} complete sampling datum of the reference signal, $d[n]$ represents the n^{th} sampled data point of the direct signal, a_{ref} is the corresponding complex amplitude, $z_{\mathrm{ref}}[n]$ is the thermal noise within the reference signal, and N is the data length which is the product of the CPI and the baseband signal sampling rate.

After converting the original surveillance signal to digital baseband, it can be expressed as

$$\begin{aligned}s_{\mathrm{sur}}[n]=&\sum_{c=1}^{N_{\mathrm{C}}}a_c d[n-\tau_c f_{\mathrm{s}}]+\sum_{m=1}^{N_{\mathrm{T}}}b_m d[n-\tau_m f_{\mathrm{s}}]\,\mathrm{e}^{\mathrm{j}2\pi f_{\mathrm{dm}}n/f_{\mathrm{s}}}\\&+z_{\mathrm{sur}}[n],\quad n=1,2,\cdots,N.\end{aligned} \tag{2}$$

Herein, f_{s} is the baseband signal sampling frequency; a_c and $\tau_c f_{\mathrm{s}}$ are the complex amplitude and range cell with respect to the direct signal of the c^{th} (c=1, 2, ⋯, N_{C}) static scattered clutter in the surveillance signal, respectively; b_m, $\tau_m f_{\mathrm{s}}$, and f_{dm} denote the complex amplitude, range cell, and Doppler frequency shift of the m^{th} (m=1, 2, ⋯, N_{T}) target in the surveillance signal, respectively; $\boldsymbol{z}_{\mathrm{sur}}$ is the thermal noise in the surveillance signal.

Based on Eqs. (1) and (2), the target detection in the PBR is performed by calculating the cross-ambiguity function (CAF) (Wu et al., 2023), which is defined as

$$\xi[r,f_{\mathrm{d}}]=\sum_{n=1}^{N}\tilde{s}_{\mathrm{sur}}[n]\,s_{\mathrm{ref}}^{*}[n-r]\,\mathrm{e}^{-\mathrm{j}2\pi f_{\mathrm{d}}n/N}, \tag{3}$$

where $r=\tau_r f_{\mathrm{s}}$ denotes the range cell of the potential target of interest and f_{d} is the corresponding Doppler frequency. $\tilde{\boldsymbol{s}}_{\mathrm{sur}}$ represents the residual surveillance signal after filtering the surveillance signal $\boldsymbol{s}_{\mathrm{sur}}$. Given $\boldsymbol{\xi}$, the CFAR detection method is implemented to derive two-dimensional detection results for the potential targets, delineated by range and Doppler.

2.2 Basic ECA and ECA-B

In the PBR's detection process, the pivotal role of clutter suppression becomes evident. We build upon the ECA approach for clutter suppression in this study. ECA projects the surveillance signal onto the signal subspace formed by the reference signal and its time-delayed counterparts, facilitating the estimation of clutter components inherent in the surveillance signal. The fundamental principle underlying this approach is expounded upon as follows:

Given $\boldsymbol{s}_{\mathrm{ref}}$, the subspace of the reference signal can be constructed as Eq. (4) (see the bottom of this page), where $K-1$ denotes the number of time-delay bins of the reference signal, and $s_{\mathrm{ref}}[-1]$, $s_{\mathrm{ref}}[-2]$, ⋯, $s_{\mathrm{ref}}[-(K-1)]$ represent the additional samples required to maintain the data length of the CPI. In practical engineering scenarios, $s_{\mathrm{ref}}[-1]$, $s_{\mathrm{ref}}[-2]$, ⋯, $s_{\mathrm{ref}}[-(K-1)]$ can be replaced by zeros, thus simplifying the implementation of ECA. Building upon the signal subspace defined in Eq. (4), the least squares method is employed to determine the weighted coefficients that minimize the residual surveillance signal metric, given by

$$\min_{\boldsymbol{\alpha}}\left\|\boldsymbol{s}_{\mathrm{sur}}-\boldsymbol{V}\boldsymbol{\alpha}\right\|^2. \tag{5}$$

By solving the least squares problem, the projection weights of ECA can be estimated as

$$\boldsymbol{\alpha}=\left(\boldsymbol{V}^{\mathrm{H}}\boldsymbol{V}\right)^{-1}\boldsymbol{V}^{\mathrm{H}}\boldsymbol{s}_{\mathrm{sur}}. \tag{6}$$

Accordingly, the residual surveillance signal after ECA is expressed as

$$\boldsymbol{V}=\begin{bmatrix}s_{\mathrm{ref}}[1] & s_{\mathrm{ref}}[-1] & s_{\mathrm{ref}}[-2] & \cdots & s_{\mathrm{ref}}[-(K-1)]\\ s_{\mathrm{ref}}[2] & s_{\mathrm{ref}}[1] & s_{\mathrm{ref}}[-1] & \cdots & s_{\mathrm{ref}}[-(K-2)]\\ s_{\mathrm{ref}}[3] & s_{\mathrm{ref}}[2] & s_{\mathrm{ref}}[1] & \cdots & s_{\mathrm{ref}}[-(K-3)]\\ \vdots & \vdots & \vdots & & \vdots\\ s_{\mathrm{ref}}[N] & s_{\mathrm{ref}}[N-1] & s_{\mathrm{ref}}[N-2] & \cdots & s_{\mathrm{ref}}[N-(K-1)]\end{bmatrix}. \tag{4}$$

$$\tilde{\boldsymbol{s}}_{\mathrm{sur}}=\boldsymbol{s}_{\mathrm{sur}}-\boldsymbol{V}\boldsymbol{\alpha}=\boldsymbol{s}_{\mathrm{sur}}-\boldsymbol{V}\left(\boldsymbol{V}^{\mathrm{H}}\boldsymbol{V}\right)^{-1}\boldsymbol{V}^{\mathrm{H}}\boldsymbol{s}_{\mathrm{sur}}. \tag{7}$$

From Eq. (7), it is evident that the computation involved in ECA primarily consists of four steps. The initial step involves the construction of the reference subspace, denoted by $\boldsymbol{V}$. This is followed by the calculation and inversion of the autocorrelation matrix, represented by $\boldsymbol{V}^{\mathrm{H}}\boldsymbol{V}$. Subsequently, the cross-correlation vector, $\boldsymbol{V}^{\mathrm{H}}\boldsymbol{s}_{\mathrm{sur}}$, is computed. Finally, the estimation of clutter is made, denoted as $\boldsymbol{V}\boldsymbol{\alpha}$. Given that the data length, N, typically ranges from tens of thousands to millions, operations associated with the reference subspace can become either too time-intensive or space-intensive. To address this concern, an approach known as ECA-B, based on data segmentation, is introduced to improve the computational efficiency of ECA. Within the framework of ECA-B, the expression for $\tilde{\boldsymbol{s}}_{\mathrm{sur}}$ is reformulated as

$$\tilde{\boldsymbol{s}}_{\mathrm{sur}}^{\mathrm{ECA\text{-}B}}=\left[\tilde{\boldsymbol{s}}_{\mathrm{ECA}_1}^{\mathrm{T}},\tilde{\boldsymbol{s}}_{\mathrm{ECA}_2}^{\mathrm{T}},\cdots,\tilde{\boldsymbol{s}}_{\mathrm{ECA}_B}^{\mathrm{T}}\right]^{\mathrm{T}} \tag{8}$$

with Eqs. (9)–(11) (see the bottom of this page and the top of the next page), where b=1, 2, ⋯, B represents the b^{th} segment of the complete data and B is the total number of segments. In practice, B is determined by the parallel processing capability of the hardware. For example, if a 16-core CPU is available, B can be set as 16, enabling each CPU to process a distinct data segment simultaneously. However, alternative values can be chosen for B. While it is theoretically feasible to execute Eq. (8) in parallel to improve the efficiency of ECA, it is worth noting, as indicated by Eq. (11), that this parallel implementation does not lead to a significant reduction in computational complexity. Instead, it just renders the process more suitable for parallel acceleration through specialized hardware. Furthermore, it should be noted that an increase in the value of B introduces periodic sidelobes in the Doppler dimension of the ECA-B results (Colone et al., 2016).

3 ECA-L based on circular convolution and circular matrix processing

In this section, we devise a method that achieves a substantial improvement in the computational efficiency of ECA, while simultaneously preserving its accuracy compared to ECA. Upon re-evaluation of Eq. (7), the principal factor contributing to the suboptimal efficiency of ECA emerges as the computation-intensive multiplication operations involving complex matrices. By substituting these resource-intensive computations with operations of lower orders, which do not incur loss, the efficiency of ECA can be markedly improved. This approach underpins the design of our ECA-L.

As highlighted in Section 2, while constructing the sliding subspace of the reference signal, it is feasible to populate $s_{\mathrm{ref}}[-1]$, $s_{\mathrm{ref}}[-2]$, ⋯, $s_{\mathrm{ref}}[-(K-1)]$ with either supplementary samples or zeros to facilitate streamlined implementation. Notably, during the sliding construction of the reference subspace, $s_{\mathrm{ref}}[-1]$, $s_{\mathrm{ref}}[-2]$, ⋯, $s_{\mathrm{ref}}[-(K-1)]$ are populated with cyclic samples derived from the surveillance signal. This choice considerably simplifies the computational intricacies while not compromising the effectiveness. Accordingly, the term $\boldsymbol{V}$ in Eq. (4) can be reformulated as Eq. (12) (see the top of the next page).

Looking at Eq. (12), it can be shown that the autocorrelation matrix corresponding to the reference subspace fits the form of a Hermitian Toeplitz matrix. This matrix is conjugate symmetric, with repeated equal elements along the main diagonal, and parallel to the main diagonal. The autocorrelation matrix can be expressed as Eq. (13) (see the top of the next page).

$$\tilde{\boldsymbol{s}}_{\mathrm{ECA}_b}=\boldsymbol{s}_{\mathrm{sur}}^{b}-\boldsymbol{V}_b\left(\boldsymbol{V}_b^{\mathrm{H}}\boldsymbol{V}_b\right)^{-1}\boldsymbol{V}_b^{\mathrm{H}}\boldsymbol{s}_{\mathrm{sur}}^{b}. \tag{9}$$

$$\boldsymbol{V}_b=\begin{bmatrix} s_{\mathrm{ref}}\left[\frac{N(b-1)}{B}+1\right] & s_{\mathrm{ref}}\left[\frac{N(b-1)}{B}\right] & \cdots & s_{\mathrm{ref}}\left[\frac{N(b-1)}{B}-(K-2)\right] \\ s_{\mathrm{ref}}\left[\frac{N(b-1)}{B}+2\right] & s_{\mathrm{ref}}\left[\frac{N(b-1)}{B}+1\right] & \cdots & s_{\mathrm{ref}}\left[\frac{N(b-1)}{B}-(K-3)\right] \\ \vdots & \vdots & & \vdots \\ s_{\mathrm{ref}}\left[\frac{bN}{B}\right] & s_{\mathrm{ref}}\left[\frac{bN}{B}-1\right] & \cdots & s_{\mathrm{ref}}\left[\frac{bN}{B}-(K-1)\right] \end{bmatrix}. \tag{10}$$

$$\boldsymbol{s}_{\mathrm{sur}}^{b}=\left[s_{\mathrm{sur}}\left[\frac{N(b-1)}{B}+1\right],s_{\mathrm{sur}}\left[\frac{N(b-1)}{B}+2\right],\cdots,s_{\mathrm{sur}}\left[\frac{bN}{B}\right]\right]^{\mathrm{T}}. \tag{11}$$

$$\boldsymbol{V}=\begin{bmatrix} s_{\mathrm{ref}}[1] & s_{\mathrm{ref}}[N] & s_{\mathrm{ref}}[N-1] & \cdots & s_{\mathrm{ref}}[N-(K-2)] \\ s_{\mathrm{ref}}[2] & s_{\mathrm{ref}}[1] & s_{\mathrm{ref}}[N] & \cdots & s_{\mathrm{ref}}[N-(K-3)] \\ s_{\mathrm{ref}}[3] & s_{\mathrm{ref}}[2] & s_{\mathrm{ref}}[1] & \cdots & s_{\mathrm{ref}}[N-(K-4)] \\ \vdots & \vdots & \vdots & & \vdots \\ s_{\mathrm{ref}}[N] & s_{\mathrm{ref}}[N-1] & s_{\mathrm{ref}}[N-2] & \cdots & s_{\mathrm{ref}}[N-(K-1)] \end{bmatrix}. \tag{12}$$

$$\boldsymbol{R}_x=\boldsymbol{V}^{\mathrm{H}}\boldsymbol{V}=\begin{bmatrix} r_x[0] & r_x[1] & r_x[2] & \cdots & r_x[K-3] & r_x[K-2] & r_x[K-1] \\ r_x^*[1] & r_x[0] & r_x[1] & \cdots & r_x[K-4] & r_x[K-3] & r_x[K-2] \\ r_x^*[2] & r_x^*[1] & r_x[0] & \cdots & r_x[K-5] & r_x[K-4] & r_x[K-3] \\ \vdots & \vdots & \vdots & & \vdots & \vdots & \vdots \\ r_x^*[K-3] & r_x^*[K-4] & r_x^*[K-5] & \cdots & r_x[0] & r_x[1] & r_x[2] \\ r_x^*[K-2] & r_x^*[K-3] & r_x^*[K-4] & \cdots & r_x^*[1] & r_x[0] & r_x[1] \\ r_x^*[K-1] & r_x^*[K-2] & r_x^*[K-3] & \cdots & r_x^*[2] & r_x^*[1] & r_x[0] \end{bmatrix}. \tag{13}$$

By referring to Eq. (13), it becomes evident that the autocorrelation matrix, denoted as $\boldsymbol{R}_x$, can be derived solely from the elements located along the first row or the first column. Furthermore, the expression for $\boldsymbol{R}_x$ can be determined as

$$\begin{aligned} r_x[k]=&\sum_{n=1}^{k}s_{\mathrm{ref}}^*[n]\,s_{\mathrm{ref}}[N-k+n] \\ &+\sum_{n=k+1}^{N}s_{\mathrm{ref}}^*[n]\,s_{\mathrm{ref}}[n-k],\ k=0,1,\cdots,K-1. \end{aligned} \tag{14}$$

To resolve Eq. (14), the following definitions are given:

$$\hat{\boldsymbol{s}}_{\mathrm{ref}}[m]=\left[s_{\mathrm{ref}}[N],s_{\mathrm{ref}}[N-1],\cdots,s_{\mathrm{ref}}[1]\right],\quad m=0,1,\cdots,N-1, \tag{15}$$

$$\boldsymbol{x}[m]=\left[s_{\mathrm{ref}}^*[1],s_{\mathrm{ref}}^*[2],\cdots,s_{\mathrm{ref}}^*[N]\right],\quad m=0,1,\cdots,N-1, \tag{16}$$

$$\boldsymbol{y}_N[m]=\left[\cdots,\hat{\boldsymbol{s}}_{\mathrm{ref}},\cdots,\hat{\boldsymbol{s}}_{\mathrm{ref}},\cdots,\hat{\boldsymbol{s}}_{\mathrm{ref}},\cdots\right],\quad m=-\infty,\cdots,+\infty, \tag{17}$$

where $\hat{\boldsymbol{s}}_{\mathrm{ref}}$ denotes the reverse sequence of $\boldsymbol{s}_{\mathrm{ref}}$, and $\boldsymbol{y}_N$ represents the periodic extension sequence of $\hat{\boldsymbol{s}}_{\mathrm{ref}}$, whose principal value sequence is equal to $\hat{\boldsymbol{s}}_{\mathrm{ref}}$. Using the aforementioned definitions and setting $K=N$, $\boldsymbol{r}_x$ in Eq. (14) can be simplified as

$$\begin{aligned} \tilde{r}_x[k]=&\sum_{m=-\infty}^{m=+\infty}\boldsymbol{x}[m]\,\boldsymbol{y}_N[k-m]=\sum_{m=0}^{N-1}\boldsymbol{x}[m]\,\boldsymbol{y}_N[k-m] \\ =&\boldsymbol{x}[m]*\boldsymbol{y}_N[m]. \end{aligned} \tag{18}$$

Eq. (18) is a standard circular convolution and $\tilde{\boldsymbol{r}}_x$ can be obtained through the linear convolution of $\boldsymbol{x}$ and the principal value sequence of $\boldsymbol{y}_N$. Moreover, the calculation of $\tilde{\boldsymbol{r}}_x$ can be simplified by the FFT, which is given by

$$\tilde{r}_x[i]=\mathrm{IFFT}\left(\mathrm{FFT}\left(\boldsymbol{s}_{\mathrm{ref}}^*\right)\mathrm{FFT}\left(\hat{\boldsymbol{s}}_{\mathrm{ref}}\right)\right),\quad i=0,1,\cdots,N-1, \tag{19}$$

where FFT(·) and IFFT(·) refer to the fast Fourier transform and inverse fast Fourier transform operations, respectively. In general, $K\ll N$, so $\boldsymbol{r}_x$ is only a subset of $\tilde{\boldsymbol{r}}_x$. Given $\tilde{\boldsymbol{r}}_x$, $\boldsymbol{r}_x$ can be expressed as

$$\boldsymbol{r}_x=\left[\tilde{r}_x[N-1],\tilde{r}_x[0],\tilde{r}_x[1],\cdots,\tilde{r}_x[K-2]\right]. \tag{20}$$

Once $\boldsymbol{r}_x$ is known, to obtain the autocorrelation matrix $\boldsymbol{R}_x$, an auxiliary term of $\boldsymbol{R}_x$ is defined as

$$\begin{aligned} \boldsymbol{r}_x^{\mathrm{aux}}=&[r_x^*[K-1],\cdots,r_x^*[2],r_x^*[1],r_x[0], \\ &r_x[1],\cdots,r_x[K-1]]. \end{aligned} \tag{21}$$

Exploiting Eq. (21), $\boldsymbol{R}_x$ is represented as

$$\boldsymbol{R}_x=\left[\boldsymbol{R}_x^{\mathrm{T}}[0],\cdots,\boldsymbol{R}_x^{\mathrm{T}}[k],\cdots,\boldsymbol{R}_x^{\mathrm{T}}[K-1]\right]^{\mathrm{T}}, \tag{22}$$

with

$$\boldsymbol{R}_x[k]=\boldsymbol{r}_x^{\mathrm{aux}}\left[(K-1-k):(2K-2-k)\right]. \quad (23)$$

Next, the inverse of $\boldsymbol{R}_x$ is computed by exploiting standard operations of Gaussian elimination or Cholesky decomposition. The cross-correlation vector ($\boldsymbol{r}_{\mathrm{c}}=\boldsymbol{V}^{\mathrm{H}}\boldsymbol{s}_{\mathrm{sur}}$) can be calculated in a similar manner. For the sake of brevity, the results of $\boldsymbol{r}_{\mathrm{c}}$ are given here with derivations omitted:

$$\boldsymbol{r}_{\mathrm{c}}=\left[\tilde{r}_{\mathrm{c}}[N-1],\tilde{r}_{\mathrm{c}}[0],\tilde{r}_{\mathrm{c}}[1],\cdots,\tilde{r}_{\mathrm{c}}[K-2]\right]^{\mathrm{T}}, \quad (24)$$

where

$$\begin{aligned}\tilde{r}_{\mathrm{c}}[i]=&\ \mathrm{IFFT}\left(\mathrm{FFT}\left(\boldsymbol{s}_{\mathrm{sur}}\right)\mathrm{FFT}\left(\hat{\boldsymbol{s}}_{\mathrm{ref}}^{*}\right)\right),\\ &i=0,1,\cdots,N-1.\end{aligned} \quad (25)$$

Given the inverse of $\boldsymbol{R}_x$, and knowing $\boldsymbol{r}_{\mathrm{c}}$, the projection weight vector of ECA-L can be obtained as

$$\boldsymbol{\alpha}=\boldsymbol{R}_x^{-1}\boldsymbol{r}_{\mathrm{c}}. \quad (26)$$

The final large-scale matrix operation involved in ECA is the estimation of clutter in the surveillance signal, that is,

$$\boldsymbol{s}_{\mathrm{sur}}^{\mathrm{c}}=\boldsymbol{V}\boldsymbol{\alpha}. \quad (27)$$

Direct computation of $\boldsymbol{V}\boldsymbol{\alpha}$ proves to be time-consuming. To streamline this process, $\boldsymbol{V}$ is initially expanded into an $N\times N$ circular matrix, while $\boldsymbol{\alpha}$ is transformed into an $N\times 1$ column vector with padding zeros. Therefore, $\boldsymbol{s}_{\mathrm{sur}}^{\mathrm{c}}$ can be further expressed as

$$\overline{\boldsymbol{s}}_{\mathrm{sur}}^{\mathrm{c}}=\boldsymbol{C}_{N\times N}\hat{\boldsymbol{\alpha}}_{N\times 1}, \quad (28)$$

with

$$\boldsymbol{C}_{N\times N}=\begin{bmatrix} s_{\mathrm{ref}}[1] & s_{\mathrm{ref}}[N] & \cdots & s_{\mathrm{ref}}[2]\\ s_{\mathrm{ref}}[2] & s_{\mathrm{ref}}[1] & \cdots & s_{\mathrm{ref}}[3]\\ \vdots & \vdots & & \vdots\\ s_{\mathrm{ref}}[N-1] & s_{\mathrm{ref}}[N-2] & \cdots & s_{\mathrm{ref}}[N]\\ s_{\mathrm{ref}}[N] & s_{\mathrm{ref}}[N-1] & \cdots & s_{\mathrm{ref}}[1] \end{bmatrix}, \quad (29)$$

$$\hat{\boldsymbol{\alpha}}_{N\times 1}=\begin{bmatrix}\boldsymbol{\alpha}_{K\times 1}\\ \boldsymbol{0}_{(N-K)\times 1}\end{bmatrix}=\left[\alpha[1],\alpha[2],\cdots,\alpha[K],0,\cdots,0\right]^{\mathrm{T}}, \quad (30)$$

where $\boldsymbol{C}$ is a cyclic matrix constructed by $\boldsymbol{s}_{\mathrm{ref}}$. It can also be readily verified that $\overline{\boldsymbol{s}}_{\mathrm{sur}}^{\mathrm{c}}$ is equivalent to $\boldsymbol{s}_{\mathrm{sur}}^{\mathrm{c}}$. Using the mathematical properties of circular matrices (Golub and van Loan, 2013), the product of the cyclic matrix $\boldsymbol{C}$ and vector $\hat{\boldsymbol{\alpha}}$ can be simplified as

$$\boldsymbol{s}_{\mathrm{sur}}^{\mathrm{c}}=\overline{\boldsymbol{s}}_{\mathrm{sur}}^{\mathrm{c}}=\boldsymbol{C}_{N\times N}\hat{\boldsymbol{\alpha}}_{N\times 1}=\mathrm{IFFT}\left(\mathrm{FFT}\left(\boldsymbol{s}_{\mathrm{ref}}\right)\mathrm{FFT}\left(\hat{\boldsymbol{\alpha}}\right)\right). \quad (31)$$

Finally, the estimated clutter, $\boldsymbol{s}_{\mathrm{sur}}^{\mathrm{c}}$, is subtracted from the surveillance signal, yielding the residual surveillance signal following clutter suppression. This is a standard operation with low computational burden. The derivation above underscores that the proposed method (ECA-L) uses simplified large-scale matrix operations (through FFT and IFFT) to streamline computations. Furthermore, there is no need to construct the reference signal's subspace. Consequently, ECA-L exhibits remarkable improvement in computational efficiency, manifesting in both temporal and spatial domains, as compared to conventional ECA or ECA-B. The flowchart of the proposed ECA-L is shown in Fig. 2, and its key implementation steps are summarized in Algorithm 1.

4 Performance, applicability, and limitation analysis

As outlined in Section 1, ECA and ECA-B are open-loop clutter suppression algorithms that are recognized for their exceptional performance, parallelizability, and applicability. Consequently, we have analyzed the performance, applicability, and limitations of both methods, in comparison to the novel ECA-L (see supplementary materials, Sections 1 and 2).

5 Simulation and field data results

Here we validate the effectiveness of the proposed ECA-L by applying it to the processing of the simulated data and field data, and comparing its results with

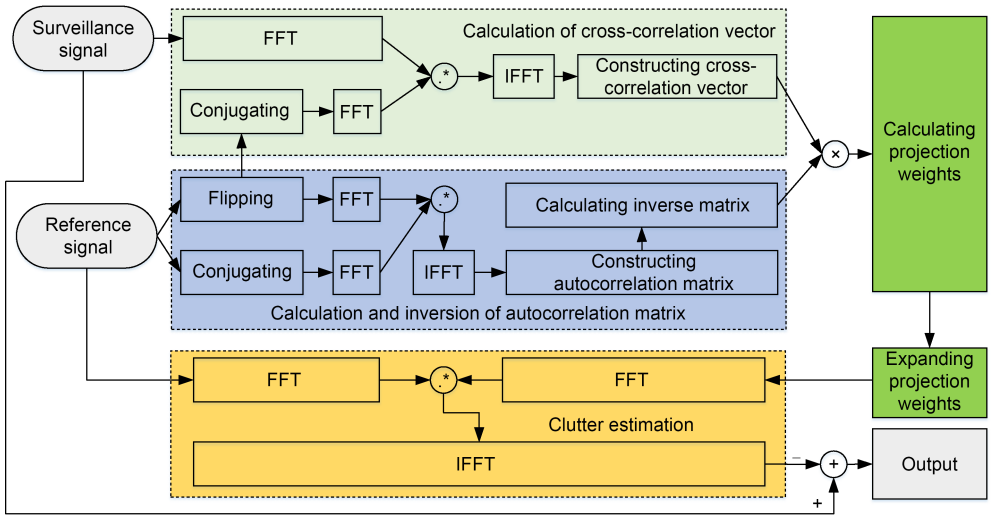

Fig. 2 Flowchart of the proposed ECA-L (FFT: fast Fourier transform; IFFT: inverse FFT)

Algorithm 1 Core steps of ECA-L

Input: original reference signal $\boldsymbol{s}_{\mathrm{ref}}\in\mathbb{C}^{N\times 1}$ and surveillance signal $\boldsymbol{s}_{\mathrm{sur}}\in\mathbb{C}^{N\times 1}$

1 Initialize the clutter suppression order, adjusting K based on the clutter level of the deployment environment. Consider setting K to 50 or greater to effectively mitigate clutter.

/* Autocorrelation matrix computation module */

2 $\tilde{r}_x[i]\leftarrow \mathrm{IFFT}\left(\mathrm{FFT}\left(\boldsymbol{s}_{\mathrm{ref}}^{*}\right)\mathrm{FFT}\left(\hat{\boldsymbol{s}}_{\mathrm{ref}}\right)\right), i=0,1,\cdots,N-1$, with $\hat{\boldsymbol{s}}_{\mathrm{ref}}=\mathrm{flipud}\left(\boldsymbol{s}_{\mathrm{ref}}\right)$

3 $\boldsymbol{r}_x\leftarrow\left[\tilde{r}_x[N-1],\tilde{r}_x[0],\tilde{r}_x[1],\cdots,\tilde{r}_x[K-2]\right]$

4 $\boldsymbol{r}_x^{\mathrm{aux}}\leftarrow[r_x^{*}[K-1],\cdots,r_x^{*}[2],r_x^{*}[1],r_x[0],r_x[1],\cdots,r_x[K-1]]$

5 $\boldsymbol{R}_x[k]\leftarrow\boldsymbol{r}_x^{\mathrm{aux}}\left[(K-1-k):(2K-2-k)\right], k=0,1,\cdots,K-1$

6 $\boldsymbol{R}_x\in\mathbb{C}^{K\times K}\leftarrow\left[\boldsymbol{R}_x^{\mathrm{T}}[0],\cdots,\boldsymbol{R}_x^{\mathrm{T}}[k],\cdots,\boldsymbol{R}_x^{\mathrm{T}}[K-1]\right]^{\mathrm{T}}$

/* Cross-correlation vector computation module */

7 $\tilde{r}_{\mathrm{c}}[i]\leftarrow\mathrm{IFFT}\left(\mathrm{FFT}\left(\boldsymbol{s}_{\mathrm{sur}}\right)\mathrm{FFT}\left(\hat{\boldsymbol{s}}_{\mathrm{ref}}^{*}\right)\right), i=0,1,\cdots,N-1$

8 $\boldsymbol{r}_{\mathrm{c}}\in\mathbb{C}^{K\times 1}\leftarrow\left[\tilde{r}_{\mathrm{c}}[N-1],\tilde{r}_{\mathrm{c}}[0],\tilde{r}_{\mathrm{c}}[1],\cdots,\tilde{r}_{\mathrm{c}}[K-2]\right]^{\mathrm{T}}$

/* Projection weights computation module */

9 $\boldsymbol{\alpha}\in\mathbb{C}^{K\times 1}\leftarrow\boldsymbol{R}_x^{-1}\boldsymbol{r}_{\mathrm{c}}$

/* Clutter estimation module */

10 $\hat{\boldsymbol{\alpha}}\in\mathbb{C}^{N\times 1}\leftarrow\left[\alpha[1],\alpha[2],\cdots,\alpha[K],0,0,\cdots,0\right]^{\mathrm{T}}$

11 $\boldsymbol{s}_{\mathrm{sur}}^{\mathrm{c}}\in\mathbb{C}^{N\times 1}\leftarrow\mathrm{IFFT}\left(\mathrm{FFT}\left(\boldsymbol{s}_{\mathrm{ref}}\right)\mathrm{FFT}\left(\hat{\boldsymbol{\alpha}}\right)\right)$

Output: clutter removal $\tilde{\boldsymbol{s}}_{\mathrm{sur}}=\boldsymbol{s}_{\mathrm{sur}}-\boldsymbol{s}_{\mathrm{sur}}^{\mathrm{c}}$

the results of traditional ECA and ECA-B. All experiments are conducted with MATLAB 2020b, using an Intel 16-core i5 processor with a clock frequency of 3.9 GHz. We use the performance evaluation metrics of average runtime over 10 trials, total allocated storage, and signal-to-noise ratio loss (SL). It is worth noting that ECA-B is considered to be fully-parallelizable when determining the average running time. In addition, with reference to the SL definition in Wang et al. (2011), the SL is quantified by the following expression:

$$\mathrm{SL}=20\lg\left(\frac{\left|\xi_{\mathrm{opt}}\left[r^{\dagger},f_{\mathrm{d}}^{\dagger}\right]\right|}{\left|\xi_{\mathrm{approx}}\left[r^{\dagger},f_{\mathrm{d}}^{\dagger}\right]\right|}\right),\tag{32}$$

where $\xi_{\mathrm{opt}}\left[r^{\dagger},f_{\mathrm{d}}^{\dagger}\right]$ and $\xi_{\mathrm{approx}}\left[r^{\dagger},f_{\mathrm{d}}^{\dagger}\right]$ represent the best-matching results of the CAF for a target after applying the optimal and suboptimal methods for clutter suppression, respectively. A smaller value for SL indicates better performance. In this section, ECA is regarded as the optimal clutter suppression method, while ECA-B and ECA-L are considered suboptimal methods.

5.1 Simulation results

A frequency modulation (FM) transmitter is used as the illuminator of opportunity for the PBR system. The main system parameters employed in processing the simulated data are described in Table 2, while comprehensive details regarding the target and clutter parameters are provided in Table 3. The overarching objective of this simulation is to demonstrate that ECA-L can achieve comparable clutter suppression performance to ECA, while reducing the runtime and storage requirements.

Table 2 System parameters of target detection

Description	Parameter	Value
Sample frequency	f_s	200 kHz
CPI	–	1 s
Clutter suppression order	K	150
Batch number (ECA-B)	B	$\{20, 40, 80, 160\}$

CPI: coherent processing interval

Table 3 Parameters of clutter and targets in the surveillance signal

Description	Range cell	Doppler frequency (Hz)
Clutter 1	1	0
Clutter 2	10	0
Clutter 3	25	0
Clutter 4	40	0
Clutter 5	83	0
Clutter 6	141	0
Target A	73	34
Target B	92	−70

The ECA, ECA-B with varying batch size, and ECA-L are used to remove the clutter within the surveillance signal. Subsequently, the CAF is executed to yield two-dimensional RD results related to targets. The Doppler dimensional profiles from the RD results for the ECA, ECA-B (across different batches), and ECA-L are presented in Fig. 3. The Doppler curves of the two targets closely overlap for both ECA and ECA-L, highlighting their comparable performance. In contrast, the performance of ECA-B diminishes as the batch size (B) increases. Moreover, Fig. 4 shows the SL and average runtime for the two targets with ECA, ECA-B, and ECA-L. It is evident that ECA-L and ECA exhibit similar performance, while ECA-B demonstrates reduced average runtime. However, ECA-B's performance is inferior to that of ECA-L. It is also important to note that ECA-B's execution often necessitates specialized hardware, such as multi-core CPUs or GPUs, unlike ECA-L. Furthermore, Fig. 5 illustrates ECA-B's tendency to produce periodic sidelobes as the number of segments increases, an issue not associated with ECA or ECA-L. Additionally, Table 4 outlines the storage allocations for the three methods, revealing ECA-B's escalating storage demands with increasing B, in contrast to ECA-L's minimal storage requirements.

In sum, compared to ECA, ECA-L attains comparable performance with notably diminished computational time and storage requirements. Furthermore, because it does not involve data segmentation, ECA-L retains high performance. Consequently, ECA-L achieves superior clutter suppression performance over ECA-B. Additionally, ECA-L's deployment is unencumbered by the hardware constraints inherent to ECA-B, which relies on specific hardware to yield greater efficiency. Moreover, ECA-L primarily relies on FFT and IFFT operations for its implementation, rendering it more amenable to parallel acceleration. Therefore, ECA-L applied with advanced hardware would be even more effective.

5.2 Field data results

In this subsection, the performance of the proposed ECA-L is verified through tests on field datasets

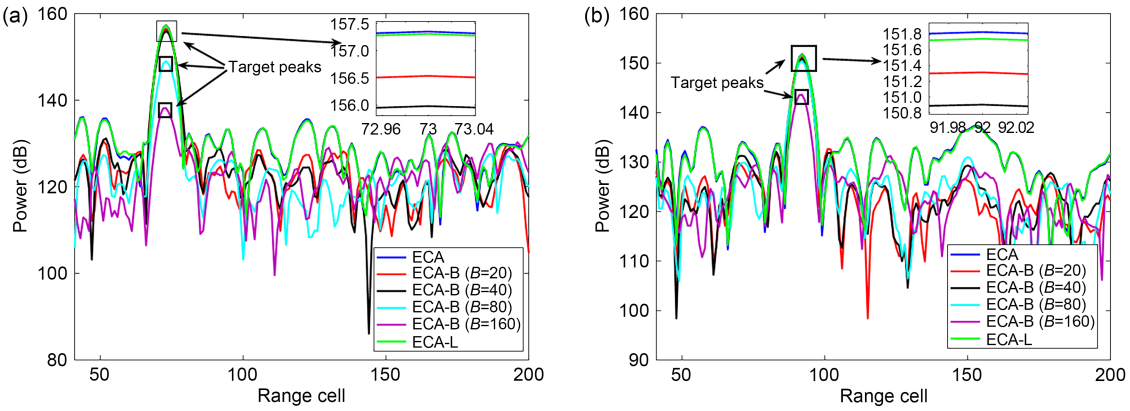

Fig. 3 Doppler dimensional profiles of the targets for ECA, ECA-B, and ECA-L: (a) Doppler dimensional profile of target A; (b) Doppler dimensional profile of target B (References to color refer to the online version of this figure)

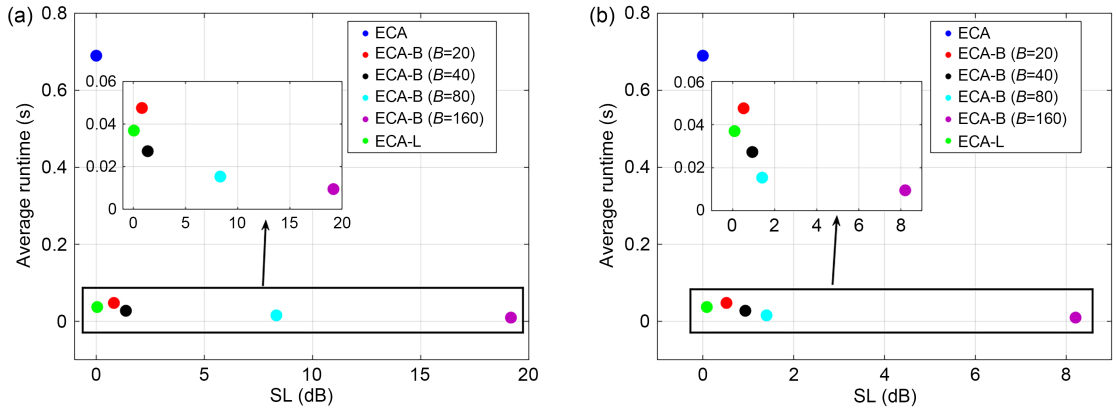

Fig. 4 Comparison of the signal-to-noise ratio loss (SL) of the two targets and average runtime for ECA, ECA-B, and ECA-L: (a) SLs of target A and average runtime for the three methods; (b) SLs of target B and average runtime for the three methods (References to color refer to the online version of this figure)

acquired with an FM transmitter and a digital television terrestrial multimedia broadcasting (DTMB) transmitter.

5.2.1 Experimental results for FM-based field data

In real-world scenarios of PBR, simultaneous multi-wave beams are a commonly used geometric configuration. This subsection uses field data obtained from an FM signal situated in Jingzhou, China, operating at a frequency of 99.6 MHz with a bandwidth of 200 kHz, to validate the effectiveness of the proposed ECA-L as compared to ECA and ECA-B. The field data are drawn from measured records of five distinct wave beams, with data from a single wave beam serving as the reference signal, and the others acting as surveillance signals. Note that more than one target is included in the field data, but in this subsection we analyze only the strongest target for simplicity. In addition, aside from changing the number of surveillance signals from one to four and configuring the clutter suppression order at 200, all remaining parameters align with those detailed in Table 2.

The target detection of measurement data including four surveillance signals can be processed in batches. Fig. 6 depicts the RD processing results of the most-representative surveillance signal with the typical ECA and CAF. Specifically, Fig. 6a portrays the top-view result, while Figs. 6b and 6c showcase the detection outcomes in the range and Doppler dimensions, respectively. A strong target is clearly discernible. Similar outcomes manifest for the remaining surveillance signals; however, for conciseness we refrain from analyzing them further. Fig. 7 displays the Doppler profile of the RD results for the strongest target, comparing the performance of the three clutter suppression methods. Additionally, Table 5 provides a comparison of average SL, average runtime, and allocated storage space for the different methods. Insights gleaned from Fig. 7 and Table 5 include: (1) ECA-L exhibits comparable performance to ECA and significantly outperforms ECA-B across varying B values. (2) Owing to its use of FFT and IFFT in lieu of matrix calculations, ECA-L's runtime is approximately an order of magnitude lower than that of ECA. While ECA-B boasts lower runtime than ECA-L, with the runtime further decreasing as B increases, such efficiency comes at the expense of performance loss. (3) ECA-L, due to its exemption from reference subspace construction, requires the least amount of storage space. (4) When evaluating performance, runtime, and storage collectively, ECA-L undoubtedly emerges as the superior of the three approaches.

5.2.2 Experimental results for DTMB-based field data

The effectiveness of the proposed ECA-L is also demonstrated with field experimental data collected from a DTMB-based PBR system. In contrast to an FM signal, the DTMB signal possesses a larger bandwidth, resulting in increased computational and storage demands on the PBR system. During the experiment, a DTMB signal originating from the Xi'an Television Tower, which operates at a frequency of 706 MHz with a bandwidth of 7.6 MHz, serves as the transmitter, while the surveillance antenna is a uniform linear array composed of eight elements. Additionally, an unmanned

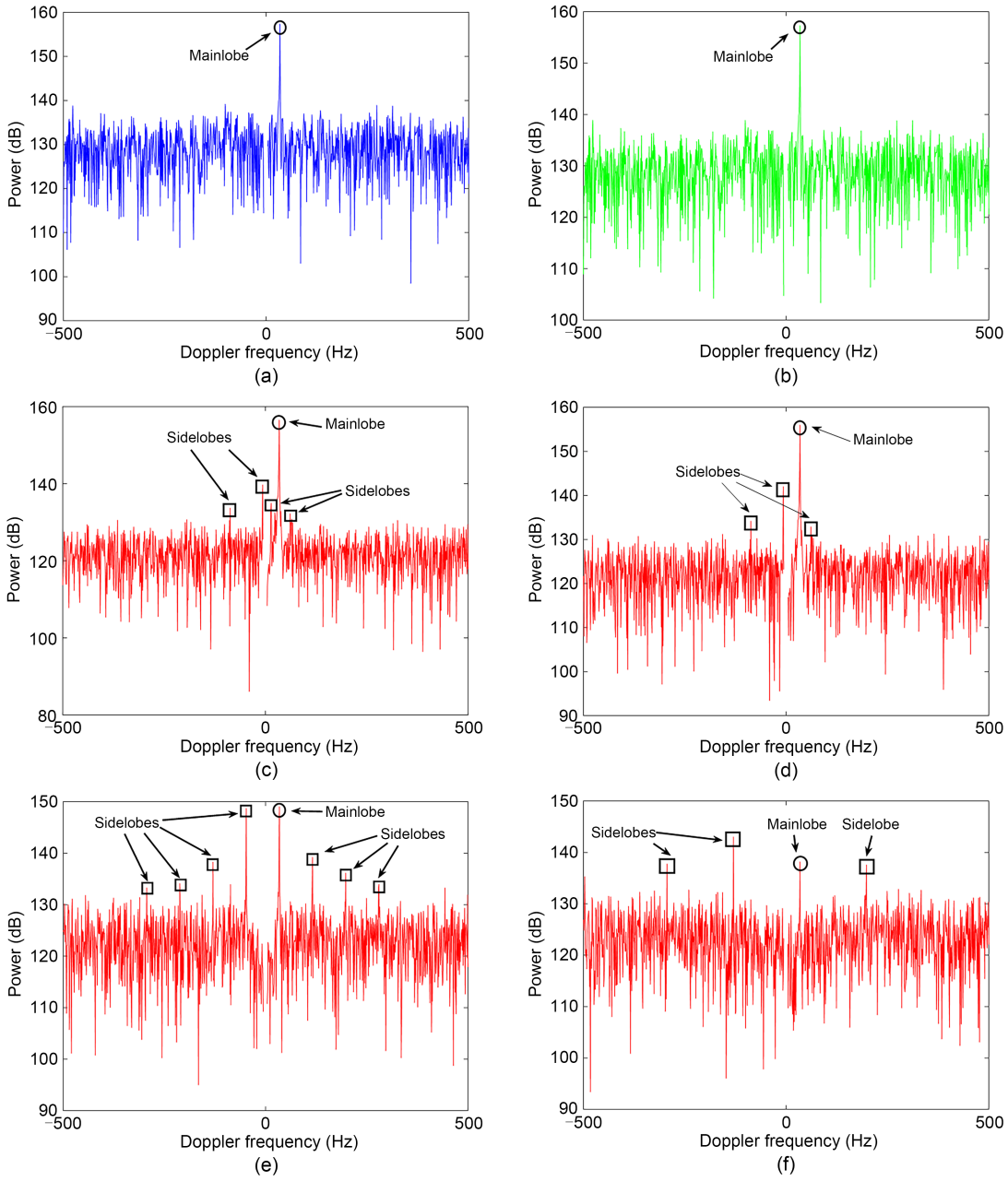

Fig. 5 Range dimensional profiles of target A for ECA (a), ECA-L (b), and ECA-B with B=20 (c), 40 (d), 80 (e), and 160 (f)

Table 4 Comparison of storage space allocated by ECA, ECA-B, and ECA-L

Algorithm	Allocated storage space (MB)
ECA	485
ECA-B (B=20)	492
ECA-B (B=40)	499
ECA-B (B=80)	513
ECA-B (B=160)	542
ECA-L	16

aerial vehicle (UAV) (DJI INSPIRE 2) is designated as the cooperative target. The DTMB-based PBR operates at a sampling rate of 8 MHz, features a CPI of 0.2 s, and employs a clutter suppression order of 250. In the experimental data, the cooperative target maneuvers near the PBR's receiving station.

The experimental data are processed using the ECA, ECA-B with varying batch size, and ECA-L methods. Fig. 8 illustrates a comparison of the RD results for the UAV target obtained through these three

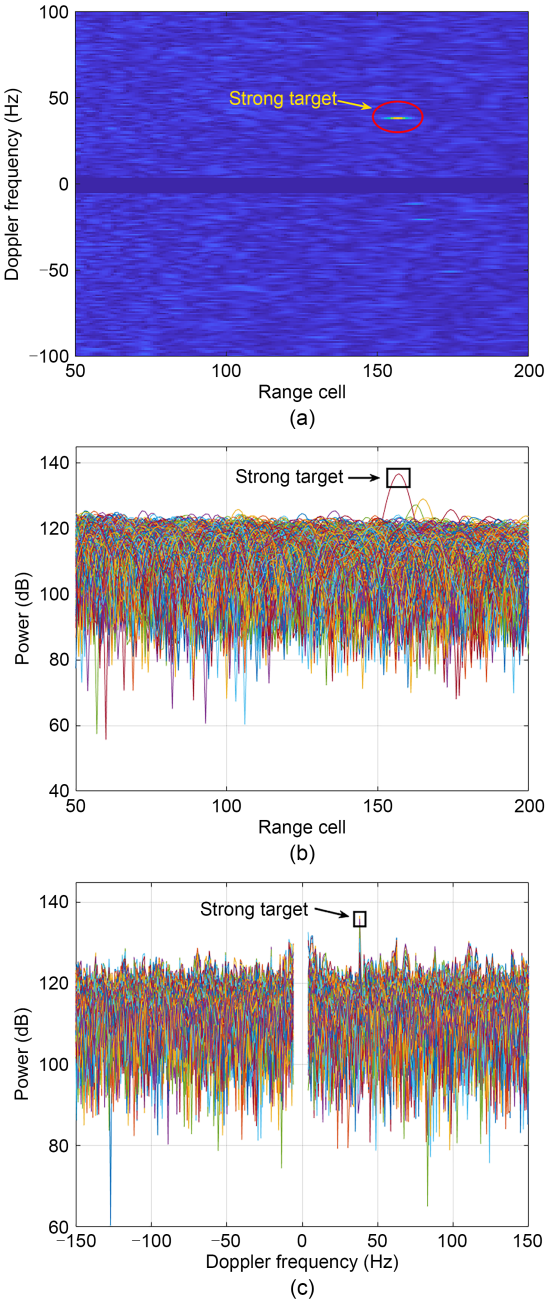

Fig. 6 Detection results of measurement data via typical range-Doppler (RD) processing: (a) result in the top view; (b) result in the range dimension; (c) result in the Doppler dimension

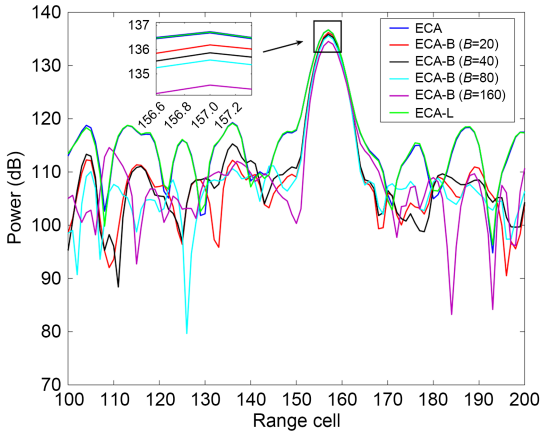

Fig. 7 Doppler dimensional profiles of the range-Doppler (RD) results of the strongest target for ECA, ECA-B, and ECA-L (References to color refer to the online version of this figure)

Table 5 Comparison of average SL, average runtime, and allocated storage space for ECA, ECA-B, and ECA-L based on FM field data

Algorithm	Average SL (dB)	Average runtime (s)	Allocated storage space (MB)
ECA	0.00	1.122	660
ECA-B (B=20)	0.66	0.075	672
ECA-B (B=40)	0.96	0.039	685
ECA-B (B=80)	1.30	0.023	711
ECA-B (B=160)	2.36	0.015	762
ECA-L	0.01	0.067	50

SL: signal-to-noise ratio loss; FM: frequency modulation

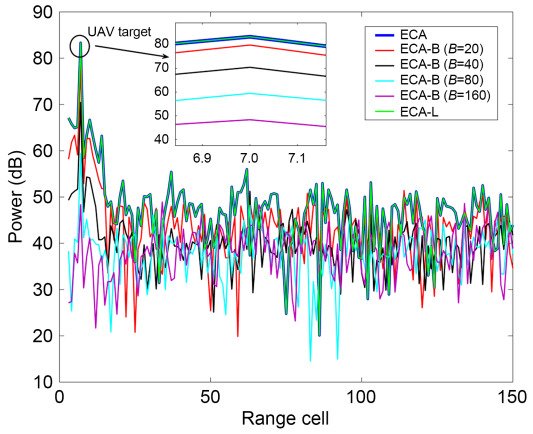

Fig. 8 Doppler dimensional profiles of the range-Doppler (RD) results of the UAV target for ECA, ECA-B, and ECA-L (References to color refer to the online version of this figure)

methods. Table 6 provides a comprehensive evaluation of these methods. Analyzing Fig. 8 and Table 6 reveals that ECA-L achieves an SL level equivalent to that of ECA, signifying comparable performance. Notably, ECA-L accomplishes this with a mere 1.5% of the runtime required by ECA, and imposes a storage requirement of only 2% of ECA's. Furthermore, when considering factors such as performance, computational time, and storage resource constraints, ECA-L exhibits significant advantages over ECA-B.

Table 6 Comparison of SL, average runtime, and allocated storage space for ECA, ECA-B, and ECA-L based on DTMB field data

Algorithm	SL (dB)	Average runtime (s)	Allocated storage space (GB)
ECA	0	19.162	6.44
ECA-B (B=20)	3.49	0.719	6.57
ECA-B (B=40)	12.89	0.348	6.59
ECA-B (B=80)	23.89	0.184	6.63
ECA-B (B=160)	35.00	0.102	6.71
ECA-L	0	0.269	0.13

SL: signal-to-noise ratio loss; DTMB: digital television terrestrial multimedia broadcasting

A noteworthy observation is the substantial memory consumption of both ECA and ECA-B, which may hinder their practical deployment. For instance, Fig. 9 displays the corresponding variations in storage requirements for all three methods when increasing the clutter suppression order from 250 to 500 in increments of 50. It is important to note that Fig. 9 depicts only the storage requirements when the batch size for ECA-B is set to 160, although this is a typical value. From Fig. 9, it is evident that even under reasonable parameters, both ECA and ECA-B demand extensive storage resources, often exceeding by several gigabytes or even surpassing by 10 GB. These requirements escalate rapidly as the clutter suppression order increases. In practical applications, high memory consumption for clutter suppression alone either is untenable or requires exorbitant hardware costs. In contrast, our proposed ECA-L requires only 2% or less of the storage

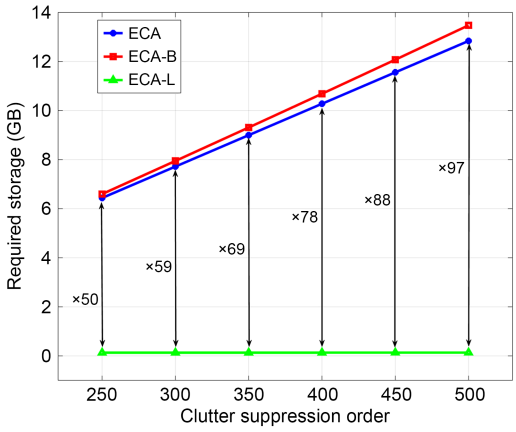

Fig. 9 Variations in storage resource requirements with clutter suppression order for ECA, ECA-B, and ECA-L

resources demanded by ECA or ECA-B to work effectively. Notably, the rate of change of the storage space required by ECA-L over different clutter suppression orders is much lower than that of ECA or ECA-B. In fact, in this example, the data length significantly exceeds the clutter suppression order, i.e., N>>K. When N is given, the space complexity of ECA-L can be considered to decrease from $O(10N+2K^2+K)$ to $O(1)$. Overall, due to significantly reduced computational and space complexities, the deployment cost of ECA-L is significantly lower than that of ECA and ECA-B. This also provides the possibility of developing better-performing clutter suppression algorithms without needing hardware upgrades.

6 Conclusions

We proposed an advanced version of ECA to mitigate inefficiencies encountered in practical applications of PBR, such as applications with large signal bandwidth or multi-source detection. Differing from mainstream batch processing methods like ECA-B and its variants (which necessitate dividing the signal and reduce the accuracy), the proposed ECA-L streamlines computations through FFT and IFFT operations and eliminates the need to divide the signal. Additionally, it dispenses with the requirement for constructing the reference subspace. As a result of these innovations, ECA-L markedly improves computational efficiency compared to traditional ECA, while maintaining comparable clutter suppression performance to ECA. The effectiveness of the proposed method was validated through both simulation and field data results, providing a valuable demonstration of its utility for PBR applications. Furthermore, it is important to note that while we mainly assessed the proposed method's performance using FM and DTMB signals, its applicability extends to other illuminators of opportunity within the PBR domain. In summation, ECA-L was demonstrated to be an accurate and efficient passive radar clutter suppression algorithm, offering potential for a broad spectrum of practical scenarios.

Contributors

Yong WU designed the research, processed the data, and drafted the paper. Luo ZUO offered data and helped organize

the paper. Dongliang PENG and Zhikun CHEN revised and finalized the paper.

Conflict of interest

All the authors declare that they have no conflict of interest.

Data availability

The data that support the findings of this study are available from the corresponding author upon reasonable request.

References

Ansari F, Taban MR, Gazor S, 2016. A novel sequential algorithm for clutter and direct signal cancellation in passive bistatic radars. *EURASIP J Adv Signal Process*, 2016:134. https://doi.org/10.1186/s13634-016-0431-2

Attalah MA, Laroussi T, Gini F, et al., 2019. Range-Doppler fast block LMS algorithm for a DVB-T-based passive bistatic radar. *Signal Image Video Process*, 13:27-34. https://doi.org/10.1007/s11760-018-1324-7

Bernaschi M, di Lallo A, Farina A, et al., 2012. Use of a graphics processing unit for passive radar signal and data processing. *IEEE Aerosp Electron Syst Mag*, 27(10):52-59. https://doi.org/10.1109/maes.2012.6373912

Bolvardi H, Derakhtian M, Sheikhi A, 2015. Reduced complexity generalised likelihood ratio detector for digital video broadcasting terrestrial-based passive radar. *IET Radar Sonar Navig*, 9(8):1021-1029. https://doi.org/10.1049/iet-rsn.2014.0557

Cardinali R, Colone F, Ferretti C, et al., 2007. Comparison of clutter and multipath cancellation techniques for passive radar. IEEE Radar Conf, p.469-474. https://doi.org/10.1109/radar.2007.374262

Colone F, O'hagan DW, Lombardo P, et al., 2009. A multistage processing algorithm for disturbance removal and target detection in passive bistatic radar. *IEEE Trans Aerosp Electron Syst*, 45(2):698-722. https://doi.org/10.1109/taes.2009.5089551

Colone F, Palmarini C, Martelli T, et al., 2016. Sliding extensive cancellation algorithm for disturbance removal in passive radar. *IEEE Trans Aerosp Electron Syst*, 52(3): 1309-1326. https://doi.org/10.1109/taes.2016.150477

Colone F, Filippini F, di Seglio M, et al., 2022. On the use of reciprocal filter against WiFi packets for passive radar. *IEEE Trans Aerosp Electron Syst*, 58(4):2746-2761. https://doi.org/10.1109/taes.2021.3138711

Colone F, Filippini F, Pastina D, 2023. Passive radar: past, present, and future challenges. *IEEE Aerosp Electron Syst Mag*, 38(1):54-69. https://doi.org/10.1109/maes.2022.3221685

Farhang-Boroujeny B, 2013. Adaptive Filters: Theory and Applications (2nd Ed.). John Wiley & Sons, Hoboken, USA, p.440-460.

Fränken D, Ott T, Lutz S, et al., 2022. Integrating multiband active and passive radar for enhanced situational awareness. *IEEE Aerosp Electron Syst Mag*, 37(8):36-49. https://doi.org/10.1109/maes.2022.3178973

Fu Y, Wan XR, Zhang X, et al., 2018. Parallel processing algorithm for multipath clutter cancellation in passive radar. *IET Radar Sonar Nav*, 12(1):121-129. https://doi.org/10.1049/iet-rsn.2017.0106

Garry JL, Baker CJ, Smith GE, 2017. Evaluation of direct signal suppression for passive radar. *IEEE Trans Geosci Remote Sens*, 55(7):3786-3799. https://doi.org/10.1109/tgrs.2017.2680321

Golub GH, van Loan CF, 2013. Matrix Computations (4th Ed.). Johns Hopkins University Press, Baltimore, USA, p.220-222.

Jarrah AA, Jamali MM, 2016a. FPGA based architecture of extensive cancellation algorithm (ECA) for passive bistatic radar (PBR). *Microprocess Microsyst*, 41:56-66. https://doi.org/10.1016/j.micpro.2015.12.003

Jarrah AA, Jamali MM, 2016b. A parallel implementation of extensive cancellation algorithm (ECA) for passive bistatic radar (PBR) on a GPU. *J Signal Process Syst*, 85(2):201-209. https://doi.org/10.1007/s11265-015-1066-5

John M, Inggs M, Petri D, 2011. Real time processing of networked passive coherent location radar system. *Int J Electron Telecommun*, 57(3):363-368. https://doi.org/10.2478/v10177-011-0049-0

Kuschel H, Cristallini D, Olsen KE, 2019. Tutorial: passive radar tutorial. *IEEE Aerosp Electron Syst Mag*, 34(2):2-19. https://doi.org/10.1109/MAES.2018.160146

Lestari AA, Simbolon L, Bura RO, et al., 2022. UWB wire-bowtie array for FM-PCL passive radar. *IEEE Trans Antenn Propag*, 70(9):7999-8007. https://doi.org/10.1109/tap.2022.3164920

Lyu X, Ding YQ, 2022. Joint multipath signals and noise reduction in passive radar. *IET Signal Process*, 16(3):366-376. https://doi.org/10.1049/sil2.12100

Mahfoudia O, Horlin F, Neyt X, 2019. Performance analysis of the reference signal reconstruction for DVB-T passive radars. *Signal Process*, 158:26-35. https://doi.org/10.1016/j.sigpro.2018.12.016

Martelli T, Colone F, Cardinali R, 2020. DVB-T based passive radar for simultaneous counter-drone operations and civil air traffic surveillance. *IET Radar Sonar Navig*, 14(4): 505-515. https://doi.org/10.1049/iet-rsn.2019.0309

Miao YJ, Li JC, Bao Y, et al., 2021. Efficient multipath clutter cancellation for UAV monitoring using DAB satellite-based PBR. *Remote Sens*, 13(17):3429. https://doi.org/10.3390/rs13173429

Moscardini C, Petri D, Capria A, et al., 2015. Batches algorithm for passive radar: a theoretical analysis. *IEEE Trans Aerosp Electron Syst*, 51(2):1475-1487. https://doi.org/10.1109/taes.2015.130407

Palmer J, Searle SJ, 2012. Evaluation of adaptive filter algorithms for clutter cancellation in passive bistatic radar. IEEE Radar Conf, p.493-498. https://doi.org/10.1109/radar.2012.6212191

Palmer J, Palumbo S, Summers A, et al., 2011. An overview of an illuminator of opportunity passive radar research project and its signal processing research directions. *Dig Signal Process*, 21(5):593-599.

https://doi.org/10.1016/j.dsp.2011.01.002

Pastina D, Santi F, Pieralice F, et al., 2021. Passive radar imaging of ship targets with GNSS signals of opportunity. *IEEE Trans Geosci Remote Sens*, 59(3):2627-2642. https://doi.org/10.1109/tgrs.2020.3005306

Samczyński P, Abratkiewicz K, Płotka M, et al., 2022. 5G network-based passive radar. *IEEE Trans Geosci Remote Sens*, 60:1-9. https://doi.org/10.1109/tgrs.2021.3137904

Sun HB, Chia LG, Razul SG, 2021. Through-wall human sensing with WiFi passive radar. *IEEE Trans Aerosp Electron Syst*, 57(4):2135-2148. https://doi.org/10.1109/taes.2021.3069767

Wang H, Wang J, Zhong L, 2011. Mismatched filter for analogue TV-based passive bistatic radar. *IET Radar Sonar Navig*, 5(5):573-581. https://doi.org/10.1049/iet-rsn.2010.0136

Wu Y, Chen ZK, Peng DL, 2023. Target detection of passive bistatic radar under the condition of impure reference signal. *Remote Sens*, 15(15):3876. https://doi.org/10.3390/rs15153876

Zhang C, Shi SZ, Yan SH, et al., 2023. Moving target detection and parameter estimation using BeiDou GEO satellites-based passive radar with short-time integration. *IEEE J Sel Top Appl Earth Obs Remote Sens*, 16:3959-3972. https://doi.org/10.1109/jstars.2023.3266875

Zuo L, Wang J, Sui J, et al., 2021. An inter-subband processing algorithm for complex clutter suppression in passive bistatic radar. *Remote Sens*, 13(23):4954. https://doi.org/10.3390/rs13234954

List of supplementary materials

1 Performance analysis

2 Applicability and limitation analysis

Table S1 Computational complexity comparisons of ECA, ECA-B, and ECA-L

Table S2 Space complexity comparisons of ECA, ECA-B, and ECA-L

Fig. S1 Computational complexity variations of ECA, ECA-B, and ECA-L over the CPI and clutter suppression order K

Fig. S2 Space complexity variations of ECA, ECA-B, and ECA-L over the CPI and clutter suppression order K